Biopotential signals of breast cancer versus tumor types and proliferation stages

Ahmed M. Hassan and Magda El-Shenawee
Department of Electrical Engineering, University of Arkansas, Fayetteville, Arkansas 72701, USA
(Received 8 September 2011; revised manuscript received 16 December 2011; published 16 February 2012)

Clinical studies have shown compelling data of elevated biopotential signals recorded noninvasively from the breasts of women with breast cancer. While these data are compelling and show a strong potential for use in the noninvasive early detection of breast cancer, there remains significant knowledge gaps which must be addressed before this technology can be routinely used for breast cancer detection. A diffusion-drift model is developed to study the spatial and temporal characteristics of the biopotential signals of breast tumors taking into account the morphology and cell division stages. The electric signals of the most common tumor types—papillary, compact, and comedo—are also considered. The largest biopotential signal is observed from the compact tumor, while the smallest signal is observed from the papillary type. The results also show an increase in the time duration of the generated biopotential signals when cancer cells start their transitions at different time instants. The spatial and temporal variations of the biopotential signals are correlated with the tumor pattern which can have important implications for breast cancer detection.

DOI: 10.1103/PhysRevE.85.021913 PACS number(s): 87.15.A−, 87.15.Vv, 87.18.Hf, 87.19.xj

I. INTRODUCTION

Breast cancer is the most common cancer diagnosed and the second leading cause of cancer-related mortality for women in the US [1]. Early detection is a key in limiting breast cancer metastasis and improving long-term survival. Advances in detection technology have helped improve 5-year survival rates from 76% in 1975 to 89% in 2010 [2]. Nevertheless, existing breast cancer screening methods suffer from substantial limitations, as recently reported in Ref. [3]. When comparing existing detection techniques alone or in combination, the highest reported sensitivity rate was 99.4% when mammography, clinical examination, and magnetic resonance imaging (MRI) were combined [3]. However, this high sensitivity was achieved at the expense of a low specificity of 7%. In sum, the combination of three techniques was able to identify accurately nearly all malignancies but was not effective in identifying healthy individuals. When combining only mammography and clinical examination, the highest overall accuracy, 75.6%, was achieved corresponding to a sensitivity of 77.4% and a specificity of 72% [3]. This level of accuracy means that one in four women may be diagnosed incorrectly, either false positive or false negative. The previous statistics show that novel and well understood detection methods are needed to improve the accuracy of breast cancer detection.

In this paper, the biopotential signals produced by breast cancer cells are investigated due to their potential use as noninvasive, passive, and low cost screening technology. Biopotential signals arise during cell division in all cells due to variations in membrane potential and ion channel activity [4]. Because cancer cells divide continuously, the measurement of electrophysiological activities, specifically biopotential signals, presents an opportunity to distinguish malignant from normal cells. Recent experimental studies at the cellular scale have measured the electrophysiological activities of breast cancer cells, using the human breast cancer cell line MCF-7 [5–9]. These studies demonstrate a prominent role for ion channels, especially potassium ion channels, in the regulation of both cell division and membrane potential. Furthermore, an increase in potassium channel expression was directly linked with tumorigenesis [8]. Finally, ras-transformed MCF-7 cells, a more malignant phenotype, exhibited larger changes in membrane potential due to hyperpolarization and larger potassium currents than conventional MCF-7 cells. Together, these observations indicate that biopotential signals provide an opportunity not only to detect breast cancer, but also to predict the degree of malignancy [9]. These cellular activities are taken into account in the diffusion-drift model to explain the biopotential signals recorded from breast cancer patients [10–20].

Several clinical studies have shown an elevation in biopotential signals recorded from the breasts of women with malignant tumors [10–20]. One preliminary study reported that combining biopotential measurements with mammography or ultrasound could potentially provide almost 100% sensitivity and 96% specificity [19]. While these data are compelling, there remain significant gaps in knowledge which must be addressed before biopotential signaling is routinely used in the detection of breast tumors. Examples of such knowledge gaps are the unknown limits of detection in terms of the smallest tumor size, the depth at which it can be detected, and the optimum location and duration of sensor placement for accurate. Furthermore, none of the preliminary clinical studies had analyzed or explained the large standard deviations observed in the recorded biopotential signals [10–20].

In order to address these knowledge gaps, we previously developed a simplified two-dimensional (2D) model that analyzed biopotential signals of a small number of MCF-7 cancer cells surrounded by plasma [21–24]. Our model was based on the diffusion and drift forces imported from semiconductor devices [21]. The model was used to simulate both the depolarization transition, where the cell membrane potential becomes more positive, and the hyperpolarization transition, where the cell membrane potential becomes more negative [22–25]. In addition, the computer parallelization of the diffusion-drift algorithm allowed the simulation of tumors composed of up to 1089 cells, as reported in Ref. [23]. However, in all our previous works, the cancerous cells were not realistically arranged to simulate a realistic tumor pattern. In this work, the most common tumor types are incorporated into the diffusion-drift model to study the effect

of tumor morphology on the generated bioelectric signals. The preliminary results of [25] show the variation of biopotential signals with the tumor pattern. In addition, the study is extended here to demonstrate a steady biopotential signal upon integrating all signals of all cancerous cells where cells divide independently.

Realistic tumor types were generated using a plethora of tumor growth models reported in the literature [26–31]. These models incorporated different factors such as the level of tumor malignancy, the interactions among the cancerous cells, and the interactions between the cancerous cells and their host environment [26–31]. These interactions included competition between cancerous and healthy cells [26,27], pressure effects due to anatomical constraints [28], contact inhibition effects, [29] and attack from the immune system [30]. These factors led to tumors of highly fractal shapes as simulated in Refs. [26] and [29]. More specifically, Ferreira *et al*. developed a reaction-diffusion tumor growth model capable of simulating various tumor morphologies such as compact, papillary, and comedo [26]. Different morphologies were achieved by incorporating different levels of competition for nutrients among the cancerous cells and the healthy cells [26]. In this work, the tumor growth model of Ferreira *et al*. [26] is utilized to generate biologically accurate tumor patterns. The current diffusion-drift model utilizes the Ferreira *et al*. model to arrange the MCF-7 cancer cells and generate tumor patterns. All cancerous cells are still immersed in plasma in this work [21–25].

This paper is organized as follows. Sec. II outlines the diffusion-drift model and Sec. III presents the numerical biopotential results for different tumor morphologies and cell division stages. Finally, the conclusions are summarized in Sec. IV. Appendix A summarizes the Ferreira *et al*. model [26], whereas Appendix B summarizes the systems of equations composing the diffusion-drift model.

II. DIFFUSION-DRIFT MODEL

Electrophysiological activities of growing cancer cells can disturb the balance of ions in the extracellular and intracellular media creating diffusion and drift forces. The following Poisson, Nernst-Plank, and continuity equations have been used to model the diffusion and drift forces in the 2D model [21–24]:

$$\nabla^2\phi = -\frac{F}{\varepsilon}\sum_m Z_m C_m, \tag{1a}$$

$$\vec{J}_m = -D_m\nabla C_m - \mu_m Z_m C_m \nabla\phi + \vec{J}a_m, \tag{1b}$$

$$\frac{\partial C_m}{\partial t} = -\nabla\cdot\vec{J}_m, \tag{1c}$$

where ϕ is the biopotential, F is Faraday's constant (96 485 C/mol), ε is the permittivity of the material ($80\varepsilon_0$ for water under quasistatic conditions), and, for each ion m, Z_m is the signed valence, C_m is the concentration, $\vec{J}_m$ is the electric current density, D_m and μ_m are the diffusion and mobility coefficients, respectively, and $\vec{J}a_m$ is the active electric current density due to ion pumps in the cell membrane. There is no known closed form solution to the above coupled equations. Therefore, numerical methods were implemented to include each term in Eq. (1), leading to a computationally expensive algorithm. Even though there are hundreds of charged ions involved in any cell, only a limited number of charged ions are hypothesized to have a significant impact on the electrophysiological activities of breast cancer cells [32]. In this work, the symbol m in Eq. (1) represents only four types of ions—potassium (C_{K+}), sodium (C_{Na+}), chloride (C_{Cl}-), and negatively charged protein (C_A-)—because of their documented impact on the membrane potential of all living cells [32].

The above equations are coupled, highly nonlinear partial differential equations [21–24]. They involve spatial as well as temporal variations that are discretized both spatially in the x and y and temporally in the time domain (t). Implicit discretization in time provided stability at the expense of high computational demands due to solving four linear systems of equations: one system for the time-dependent biopotential and three systems for three ions. The implicit temporal discretization of (1) for the biopotentialϕcan be expressed as [21–24]

$$\nabla^2\phi^{t+1} = -\frac{F}{\varepsilon}\sum_m Z_m\left(C_m^t - \Delta t\vec{\nabla}\cdot\vec{J}_m^{t,t+1}\right), \tag{2a}$$

$$\frac{C_m^{t+1}-C_m^t}{\Delta t} = -\vec{\nabla}\cdot\vec{J}_m^{t+1} = \vec{\nabla}\cdot\left(D_m\vec{\nabla}C_m^{t+1} + \mu_m C_m^{t+1} Z_m\nabla\phi^{t+1} - \vec{J}a_m\right), \tag{2b}$$

where the update in time is represented by $(t+1)$. Notice that the last term in Eq. (2a) provides the stability to the temporal discretization. The present model uses nonuniform spatial discretization of both the 2D intracellular and extracellular domains due to the contrast in size in the different spatial scales in the model. For example, the gap between cells is almost 10 times smaller than the cell size [22]. The spatial discretization of the biopotential is expressed at pixel (i,j) as

$$\nabla^2\phi^{t+1}(i,j) = \partial^2\phi^{t+1}(i,j)/\partial x^2 + \partial^2\phi^{t+1}(i,j)/\partial y^2, \tag{3}$$

where the derivative terms with respect to x and y are expressed as functions of the neighboring pixels $(i-1,i+1,j-1,j+1)$ [21–24]. Nonuniform spatial discretization is evoked to efficiently handle the contrast in size between the different features in the model. For example, the average intercellular spacing is more than an order of magnitude smaller than the cell size [22–24]. Once spatially discretized (2) can be expressed as

$$\nabla^2\phi^{t+1}(i,j) = \partial^2\phi^{t+1}(i,j)/\partial x^2 + \partial^2\phi^{t+1}(i,j)/\partial y^2 = \frac{2}{h_{i,_j}+h_{i,j+1}}\left[\frac{\phi^{t+1}(i,j+1)}{h_{i,j+1}} + \frac{\phi^{t+1}(i,j-1)}{h_{i,j}} - \phi^{t+1}(i,j)\frac{h_{i,j}+h_{i,j+1}}{h_{i,j}h_{i,j+1}}\right] + \frac{2}{g_{i,_j}+g_{i+1,j}}\left[\frac{\phi^{t+1}(i+1,j)}{g_{i+1,j}} + \frac{\phi^{t+1}(i-1,j)}{g_{i,j}} - \phi^{t+1}(i,j)\frac{g_{i,j}+g_{i+1,j}}{g_{i,j}g_{i+1,j}}\right], \tag{4a}$$

and

$$\vec{\nabla}\cdot\vec{J}_m^{t,t+1} = [J_{xm}(i,j+0.5) - J_{xm}(i,j-0.5)]/[(h_{i,j}+h_{i,j+1})/2] + [J_{ym}(i+0.5,j) - J_{ym}(i-0.5,j)]/[(g_{i,j}+g_{i+1,j})/2], \quad (4b)$$

$$J_{xm}(i,j+0.5) = -D_m(i,j+0.5)\left[C_m^t(i,j+1) - C_m^t(i,j)\right]/h_{i,j+1} - Z_m\mu_m(i,j+0.5)C_m^t(i,j+0.5)[\phi^{t+1}(i,j+1) - \phi^{t+1}(i,j)]/h_{i,j+1} + J_{a_{xm}}(i,j+0.5), \quad (4c)$$

$$J_{xm}(i,j-0.5) = -D_m(i,j-0.5)\left[C_m^t(i,j) - C_m^t(i,j-1)\right]/h_{i,j} - Z_m\mu_m(i,j-0.5)C_m^t(i,j-0.5)[\phi^{t+1}(i,j) - \phi^{t+1}(i,j-1)]/h_{i,j} + J_{a_{xm}}(i,j-0.5), \quad (4d)$$

where $h_{i,_{j+1}} = x_{i,j+1} - x_{i,j}, h_{i,j} = x_{i,j} - x_{i,j-1}$, and $x_{i,j}$, $x_{i,j+1}$, $x_{i,j-1}$ represent the x coordinates of the grid points (i,j), $(i,j+1)$, and $(i,j-1)$, respectively, and $g_{i+1,_j} = y_{i+1,j} - y_{i,j}$, $g_{i,j} = y_{i,j} - y_{i-1,j}$, and $y_{i,j}$, $y_{i+1,j}$, and $y_{i-1,j}$ represent the y coordinates of the grid points (i,j), $(i+1,j)$, and $(i-1, j)$, respectively. Similar equations to (4c) and (4d) are obtained for J_{ym}. Upon regrouping all discretized terms in time and space, four linear systems of equations are produced for the biopotential ϕ, potassium C_{K^+}, chloride C_{Cl^-}, and sodiumC_{Na^+} concentrations as [23]

$$A_\phi v_\phi = b_\phi, \quad (5a)$$

$$A_{K^+} v_{K^+} = b_{K^+}, \quad (5b)$$

$$A_{Cl^-} v_{Cl^-} = b_{Cl^-}, \quad (5c)$$

$$A_{Na^+} v_{Na^+} = b_{Na^+}, \quad (5d)$$

where $v_\phi, v_{K^+}, v_{Na^+}, v_{Cl^-}$ are the biopotential, concentration of potassium ions, concentration of sodium ions, and concentration of chloride ions, respectively, at each grid point in the computational domain. The entries of the systems of equations in Eq. (5) are expressed explicitly in Appendix B. Since proteins cannot penetrate the cell membrane, in this work their concentration is assumed fixed at 135 mM [21,22]. Therefore, there is no relation for the motion of proteins C_A- via the diffusion or the drift forces. However, the effect of the negatively charged proteins C_A- is incorporated in all

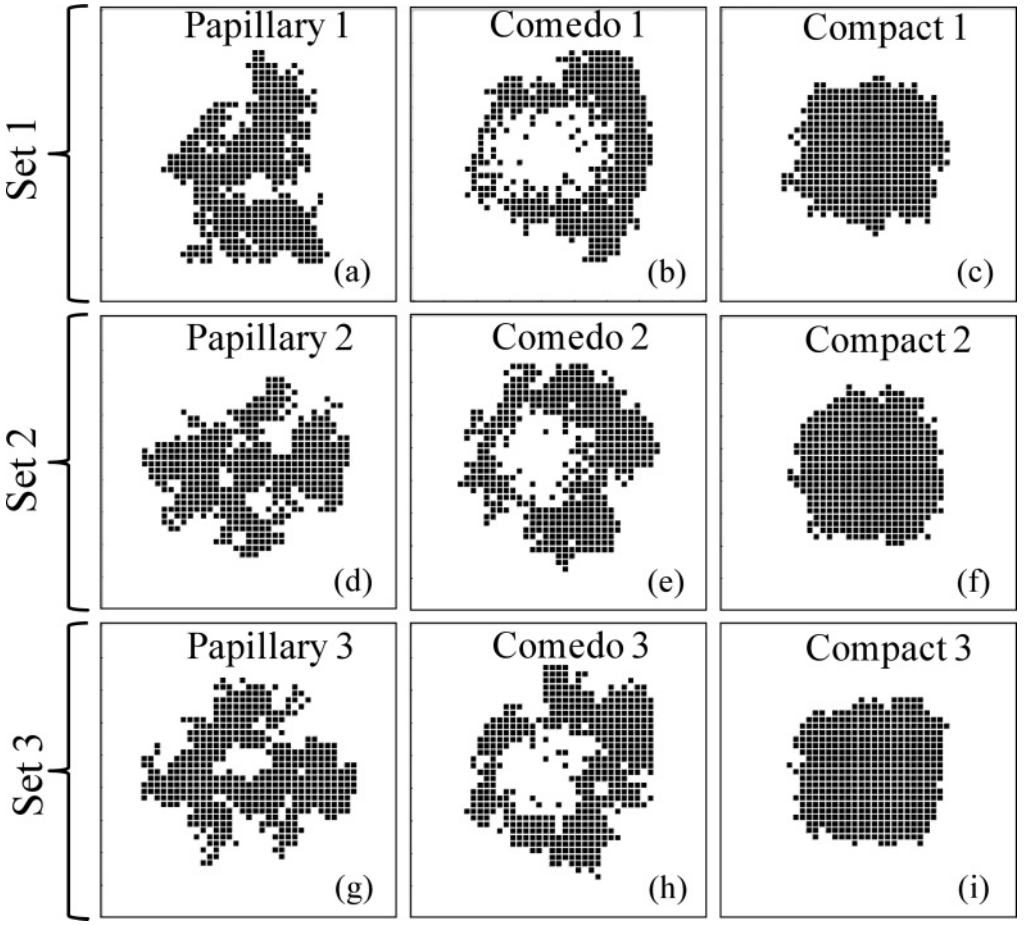

FIG. 1. (a) First papillary tumor pattern, (b) first comedo tumor pattern, (c) first compact tumor pattern, (d) second papillary tumor pattern, (e) second comedo tumor pattern, (f) second compact tumor pattern, (d) third papillary tumor pattern, (e) third comedo tumor pattern, (f) third compact tumor pattern.

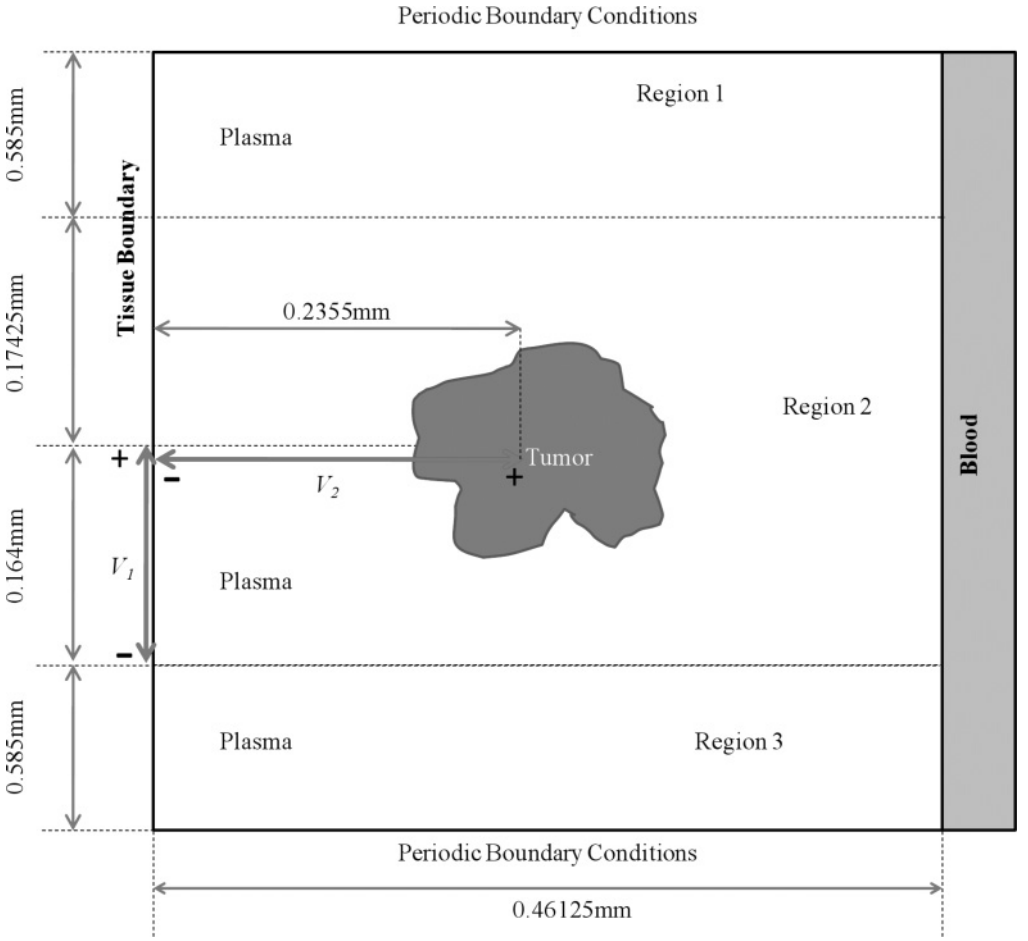

FIG. 2. The computational domain showing the locations of the biopotentials V_1 and V_2.

calculations as indicated in Eq. (1), where m represents all four ions considered in this work, including the negatively charged proteins.

Each cancer cell's semipermeable membrane contains active ion pumps and ion channels whose activities vary with the cell division stage. Upon opening and closing the membrane channels, its permeability varies with the division stage. During the cell division cycle, membrane potentials exhibit either depolarization or hyperpolarization [5]. The depolarization of the membrane of MCF-7 cell typically occurs at the beginning of the G1 stage of the cell division cycle, whereas the hyperpolarization occurs at the G1/S transition of the cycle [5]. The 2D model accounted for both depolarization and hyperpolarization when calculating the biopotential signals. The variations in the membrane potential can be attributed to changes in the permeability of the cell membrane to certain ions in addition to variations in the active currents due to ion pumps at the membrane. For example, the permeability of the MCF-7 cell membrane to potassium ions was found to increase by a factor of 10 during the hyperpolarization stage which occurs in the G1/S transition [6]. The active current due to the ion pumps at the cell membrane was found to increase during the G1/S transition of neuroblastoma cancer cells [33,34]. The previously described changes in the permeability of the cell membrane to potassium ions and the level of the active current densities are used together with Eqs. (1)–(4) to simulate the depolarization and hyperpolarization.

III. NUMERICAL RESULTS

In order to reduce the computational time, the solution of the four systems of equations (4) is parallelized using the Portable, Extensible Toolkit for Scientific Computation (PETSc) library, as discussed in Ref. [23]. All of the results in this paper are generated using the parallelized code developed in Ref. [23] and executed using 56 processors on the Star of Arkansas supercomputer. The Star of Arkansas consists of 157 nodes each with dual quad-core Xeon E5430 processors, 2×6 MB cache, 2.66 GHz, 1333FSB. The Star of Arkansas has 1256 available cores and each core has 2 GB of memory. Three tumor types—*papillary*, *compact,* and *comedo,* which is a tumor with a central necrotic core—are generated using the Ferreira *et al*. model and adapted for the diffusion-drift model as detailed in Appendix A [26].

Nine tumor patterns are simulated here, where each of the three patterns belong to one tumor type (i.e., papillary, compact, or comedo). For each of the nine tumor patterns, six different distributions of cell division stages are

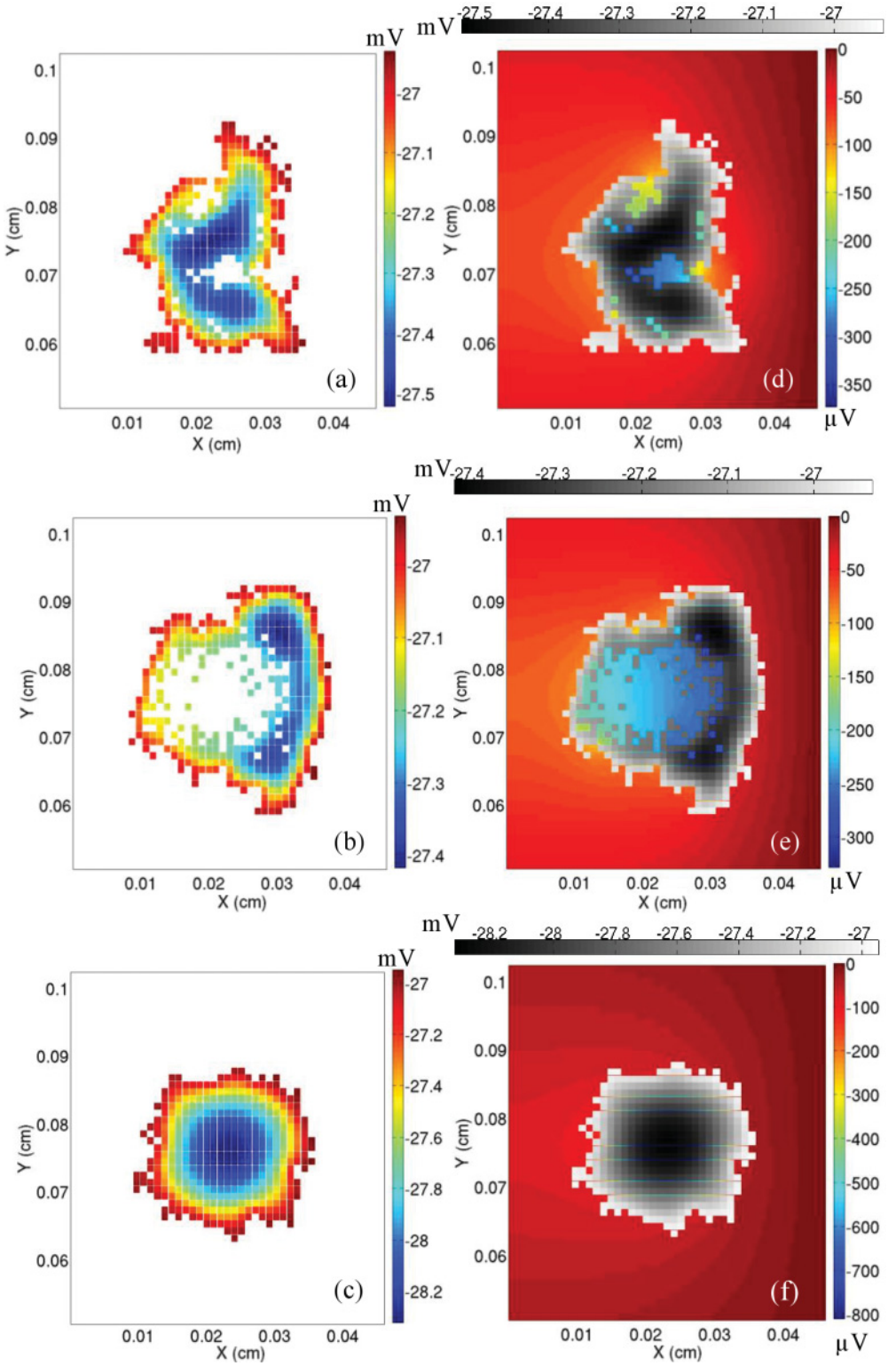

FIG. 3. (Color) The spatial distribution of the intracellular biopotentials for Set 1 and Case 1 for the (a) first papillary pattern, (b) first comedo pattern, and (c) first compact pattern and the spatial distribution of the intracellular and extracellular biopotentials for Set 1 and Case 1 for the (d) first papillary pattern, (e) first comedo pattern, and (f) first compact pattern. All 444 cells are depolarizing.

considered. A total of 54 cases, are simulated in this work. Due to computational resource limitations, only 444 cancerous MCF-7 cells are considered in each tumor pattern. Set 1 is shown in Figs. 1(a)–1(c), Set 2 is shown in Figs. 1(d)–1(f), and Set 3 is shown in Figs. 1(g)–1(i). The spatiotemporal characteristics of the biopotential signals generated from these three sets of tumor patterns are discussed in the following sections.

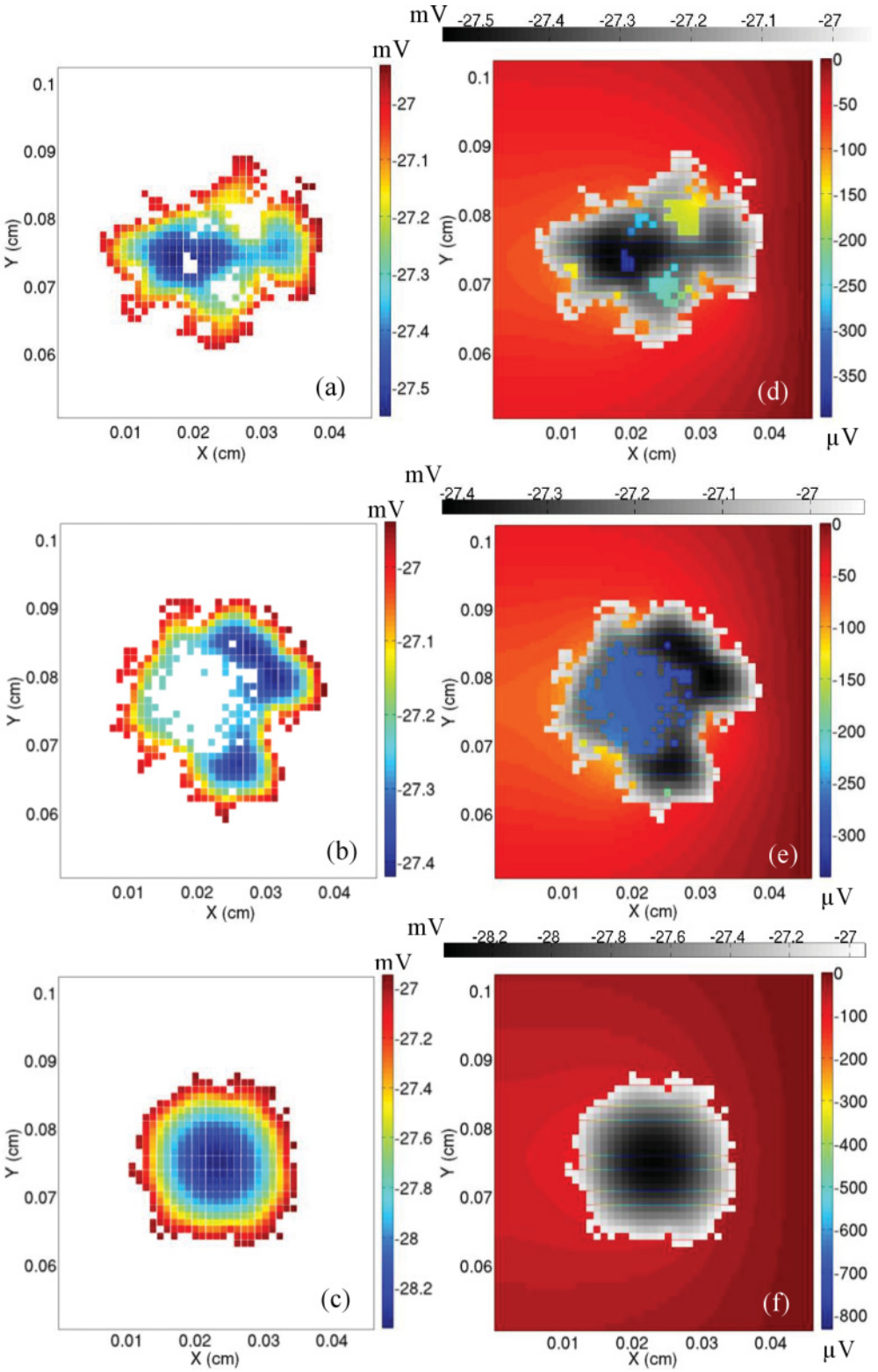

FIG. 4. (Color) The spatial distribution of the intracellular biopotentials for Set 2 and Case 1 for the (a) second papillary pattern, (b) second comedo pattern, and (c) second compact pattern and the spatial distribution of the intracellular and extracellular biopotentials for Set 2 and Case 1 for the (d) second papillary pattern, (e) second comedo pattern, and (f) second compact pattern. All 444 cells are depolarizing.

A. Spatial biopotential patterns

The computational domain shown in Fig. 2 is utilized in simulating the biopotential signals generated by the tumor patterns in Fig. 1. The computational domain consists of 450×450 pixels and all the patterns in Fig. 1 are centered at the center of the computational domain in Fig. 2. The regions

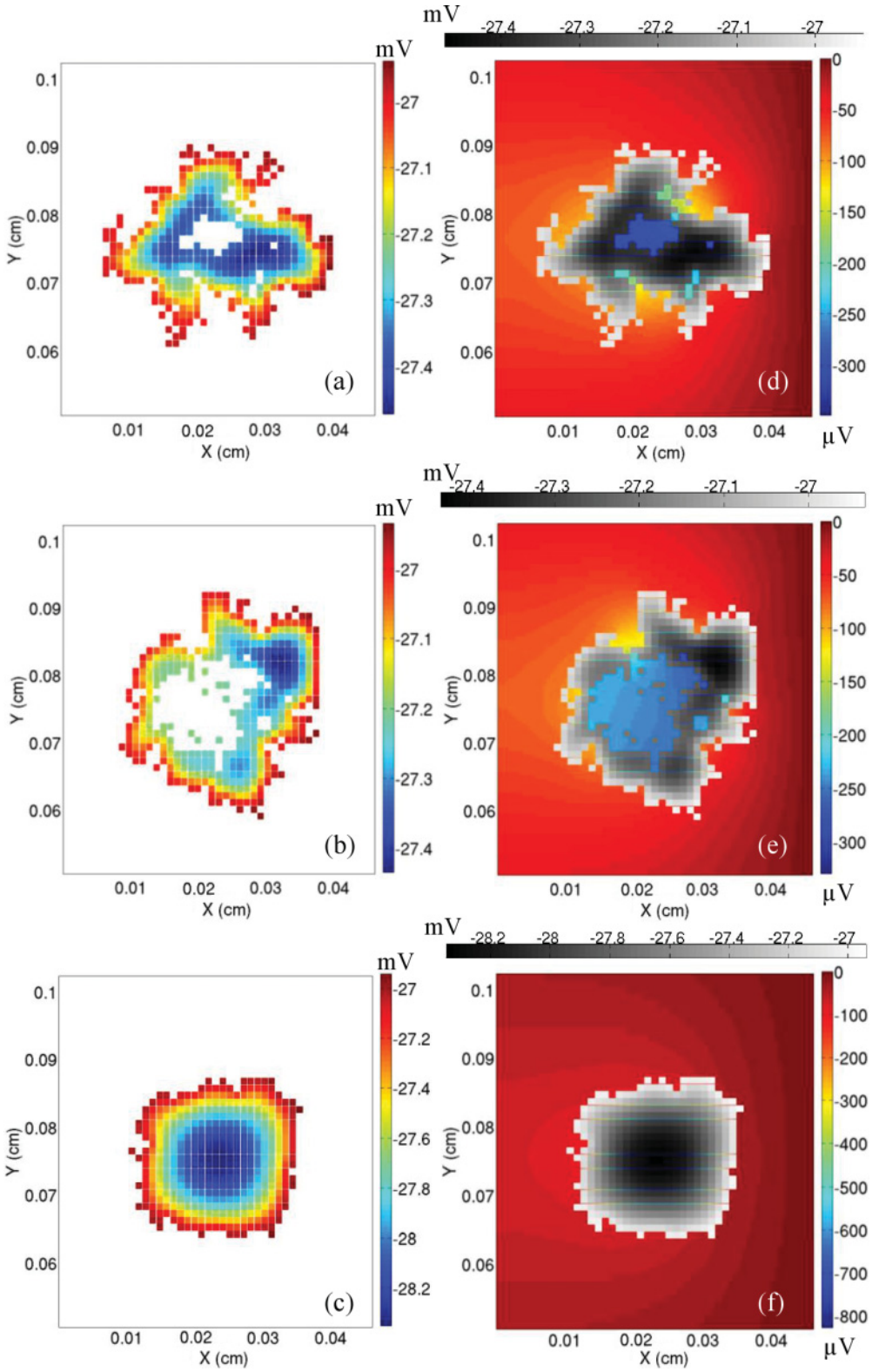

FIG. 5. (Color) The spatial distribution of the intracellular biopotentials for Set 3 and Case 1 for the (a) third papillary pattern, (b) third comedo pattern, and (c) third compact pattern and the spatial distribution of the intracellular and extracellular biopotentials for Set 3 and Case 1 for the (d) third papillary pattern, (e) third comedo pattern, and (f) third compact pattern. All 444 cells are depolarizing.

of the computational domain where no cancerous cells exist are filled with plasma including the intercellular spacing. In the comedo type, where dead cells exist in the center, the center is also filled with plasma. In reality, the necrotic core is filled with dead cancerous cells and enzymes secreted to break down the dead cancerous cells [31]. This mixture is modeled as plasma as a first order approximation to the mixture in the necrotic core.

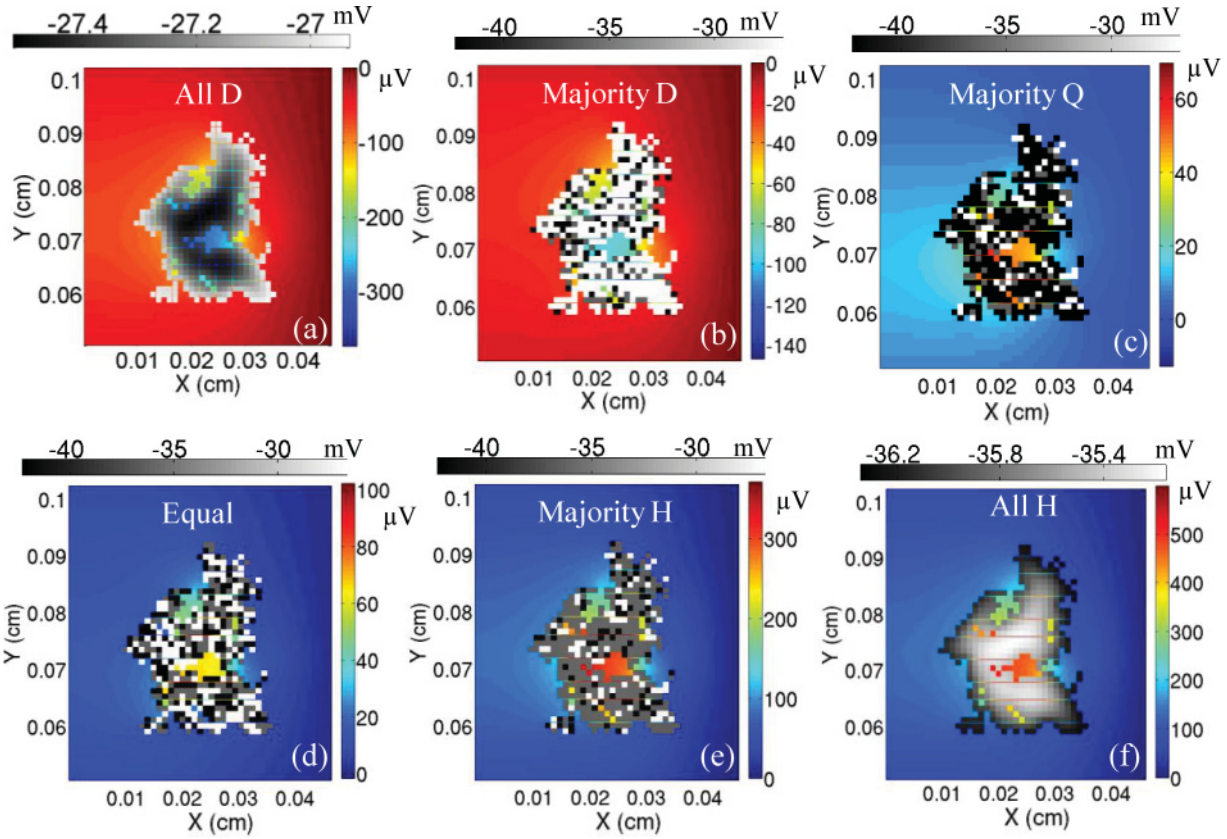

FIG. 6. (Color) The spatial distribution of the intracellular and extracellular biopotentials for the first papillary pattern for the six cases: (a) where all the cells are depolarizing, (b) where the majority of the cells are depolarizing, (c) where the majority of the cells are quiescent, (d) where the cells are equally distributed between the depolarization, hyperpolarization, and quiescent stages, (e) where the majority of the cells are hyperpolarizing, and (f) where all the cells are hyperpolarizing. Total number of cells is 444 in each figure.

There are three main membrane potential transitions incorporated in this work: (i) depolarization (D), (ii) hyperpolarization (H), and (iii) quiescence (Q). The first case considered, Case 1, considers all cells as depolarizing. The results in Figs. 3, 4, and 5 are obtained upon running the diffusion-drift algorithm for 49 s from the start of the depolarization transition for tumor Set 1 [Figs. 1(a)–1(c)], Set 2 [Figs. 1(d)–1(f)], and Set 3 [Figs. 1(g)–1(i)], respectively. Figures 3(a)–3(c) show the intracellular biopotential, which is the biopotential inside the cancerous cells. Figures 3(d)–3(f) show both the intracellular and the extracellular biopotentials where the intracellular biopotential is shown in shades of gray, while the extracellular biopotential is shown in color. Due to the large contrast in the magnitude of the biopotentials inside and outside the cells, two color scales are used in Figs. 3(d)–3(f). The color bars show that the magnitudes of the intracellular biopotentials are significantly larger than the magnitudes of the extracellular biopotentials. The reference zero biopotential for all plots is the blood vessel at the right hand side of the computational domain in Fig. 2. Similar plots are shown in Figs. 4 and 5 but for the tumor Sets 2 and 3, respectively.

In the depolarization transition, the intracellular biopotential becomes more positive, changing from −42.3 to −15 mV [21]. Figures 3(a)–3(c) demonstrated that the cancerous cells at the outer rim of the tumor are more positive than the cancerous cells in the interior of the tumor. Therefore, the transition is slightly faster in the cells on the outer rim of the tumor than in the cells in the interior of the tumor, which is also observed in Figs. 3(b) and 3(c). This faster transition can be explained by the fact that the cells at the outer rim of the tumor have

TABLE I. Description of Cases 1–6.

Case	Description
Case 1	All cells are depolarizing
Case 2	66.6% of the cells are depolarizing, 16.6% of the cells are hyperpolarizing, 16.6% of the cells are quiescent
Case 3	66.6% of the cells are quiescent, 16.6% of the cells are depolarizing, 16.6% of the cells are hyperpolarizing
Case 4	33% of the cells are depolarizing, 33% of the cells are hyperpolarizing, 33% of the cells are quiescent
Case 5	66.6% of the cells are hyperpolarizing, 16.6% of the cells are depolarizing, 16.6% of the cells are quiescent
Case 6	All cells are hyperpolarizing

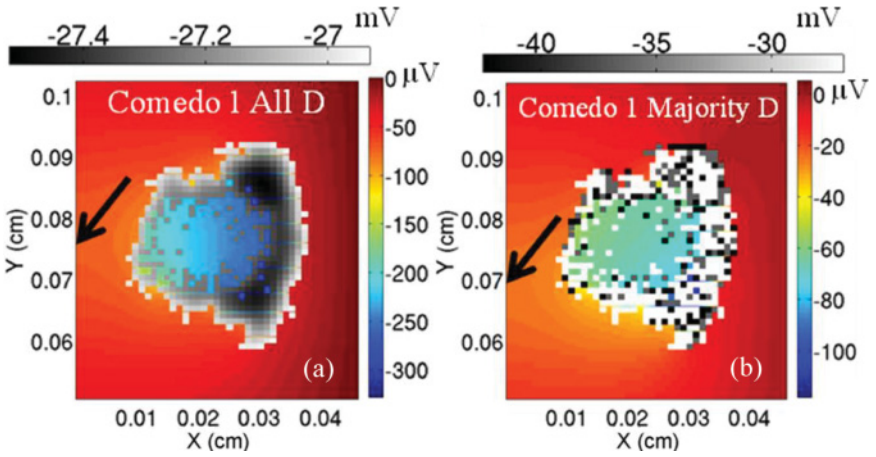

FIG. 7. (Color) The spatial distribution of the intracellular and extracellular biopotentials for the (a) first comedo pattern for the case where all the cells are depolarizing and (b) first comedo pattern for the case where the majority of the cells are depolarizing. The point of maximum biopotential at the tissue boundary ($x = 0$) is marked with a black arrow. Total number of cells is 444 in each figure.

more access to the extracellular plasma and, therefore, any ions released by these cells disperse faster clearing the way for more ions to be dispersed by the cells.

In Fig. 3(d), the magnitude of the biopotential in the gaps between the fingerlike protrusions of the tumor pattern is significantly high (negative in sign). This is because any ions released in those gaps have their motion restricted by the surrounding cell boundaries and, therefore, the ions accumulate causing the magnitude of the biopotentials to increase. The same explanation can be used to explain why the biopotential is large in the necrotic core in Fig. 3(e) since the ions released in the necrotic core have their motion restricted by the cells in the outer rim of the tumor. As for the compact pattern in Fig. 3(f), the maximum extracellular biopotential is in the intracellular spacing surrounding the MCF-7 cells in the center of the tumor and it decreases gradually in the intercellular spacing toward the boundary of the tumor. Upon comparing the magnitudes of the extracellular biopotentials in the color bars in Figs. 3(d)–3(f), it can be seen that the compact tumor shape generates the largest extracellular biopotential. This can be explained by the fact that most of the cells in the compact pattern have only access to the extracellular plasma in the small intercellular spacing and, therefore, the ions released by the cells have their motion significantly reduced. The papillary pattern has substantial access to plasma caused by the increase in the surface area to volume ratio resulting from its fractal shape. For the comedo pattern, most of the cells have access to the plasma in the necrotic core, which causes the generated extracellular biopotential to be lower than those generated from the compact pattern.

The same trend between the generated biopotentials and the tumor morphology can be seen in the different patterns in Fig. 4 for Set 2 and in Fig. 5 for Set 3. Upon comparing all results in Figs. 3–5, it can be seen that different tumor patterns generate different spatial variations in biopotential signals. The differences are especially clear in the vicinity of the tumor. Comparing the results in Fig. 3(e) with those in Fig. 4(e), it can be seen that the extracellular biopotential in the necrotic core in Fig. 4(e) is larger in magnitude than that in the necrotic core in Fig. 3(e). This can be explained by the fact that the necrotic core in Fig. 4(e) is smaller than the one in Fig. 3(e) and, therefore, the motion of the ions dissipated by the cells is more restricted in this case.

The cell division cycle can be divided into G0, G1, S, G2, and M stages. The G0 stage is a dormant stage that the cell enters before or after the division is completed. In the G1 stage, the cell grows and the proteins and RNA are synthesized, whereas in the S stage, the chromosome replication occurs. The cell growth continues in the G2 stage, which also acts as the final checkpoint before the cell divides in the mitosis or the M stage. In this work, all cells were assumed to be simultaneously depolarizing; therefore, they are in the same cell division stage. However, in a growing tumor, it is more likely that cells divide independently [35]. Moreover, at different stages of tumor growth, the cancerous cells favor a certain cell division stage more than the other [35]. Typically, tumors exhibit an initial exponential growing phase followed by a plateau growing phase. In the *in vitro* study in Ref. [35], MCF-7 cells composing a tumor in an exponential growing phase were found to be divided among the cell division stages as follows: $48.9 \pm 0.6\%$ of cells were in G0-G1, $39.4 \pm 0.6\%$ were in S, and $11.6 \pm 0.3\%$ were in G2+M phase. However, in the plateau growing phase the distribution of the MCF-7 cells changed as follows: $74.8 \pm 0.7\%$ of cells were in G0-G1, $15.3 \pm 0.4\%$ were in S, and $9.8 \pm 0.6\%$ were in G2+M phase. In addition, as the size of the tumor increases, the majority of the cells are in the quiescent state, and only a small fraction of the cells are dividing. These reports imply that only a minority of the cells will be depolarizing or hyperpolarizing.

To investigate the effect of different cell division stages, five additional cases are simulated as illustrated in Figs. 6(a)–6(f) for the first papillary pattern shown in Fig. 1(a). For convenience, the cases are summarized in Table I. Figure 6(a) shows the previously described Case 1, where all cells are depolarizing. Figure 6(b) shows Case 2, where the majority of cells are set to depolarize by setting the probability of cells depolarizing to 66.6%, the probability of cells hyperpolarizing to 16.6%, and the probability of cells quiescent to 16.6%. Figure 6(c) shows Case 3 where the majority of cells are set to be quiescent by setting the probability of cells quiescent to 66.6%, the probability of cells depolarizing to 16.6%, and the probability of cells hyperpolarizing to 16.6%. Figure 6(d) shows Case 4, where cells are equally distributed among the different transitions such that the probability of a cell depolarizing, hyperpolarizing or quiescent is set equal to

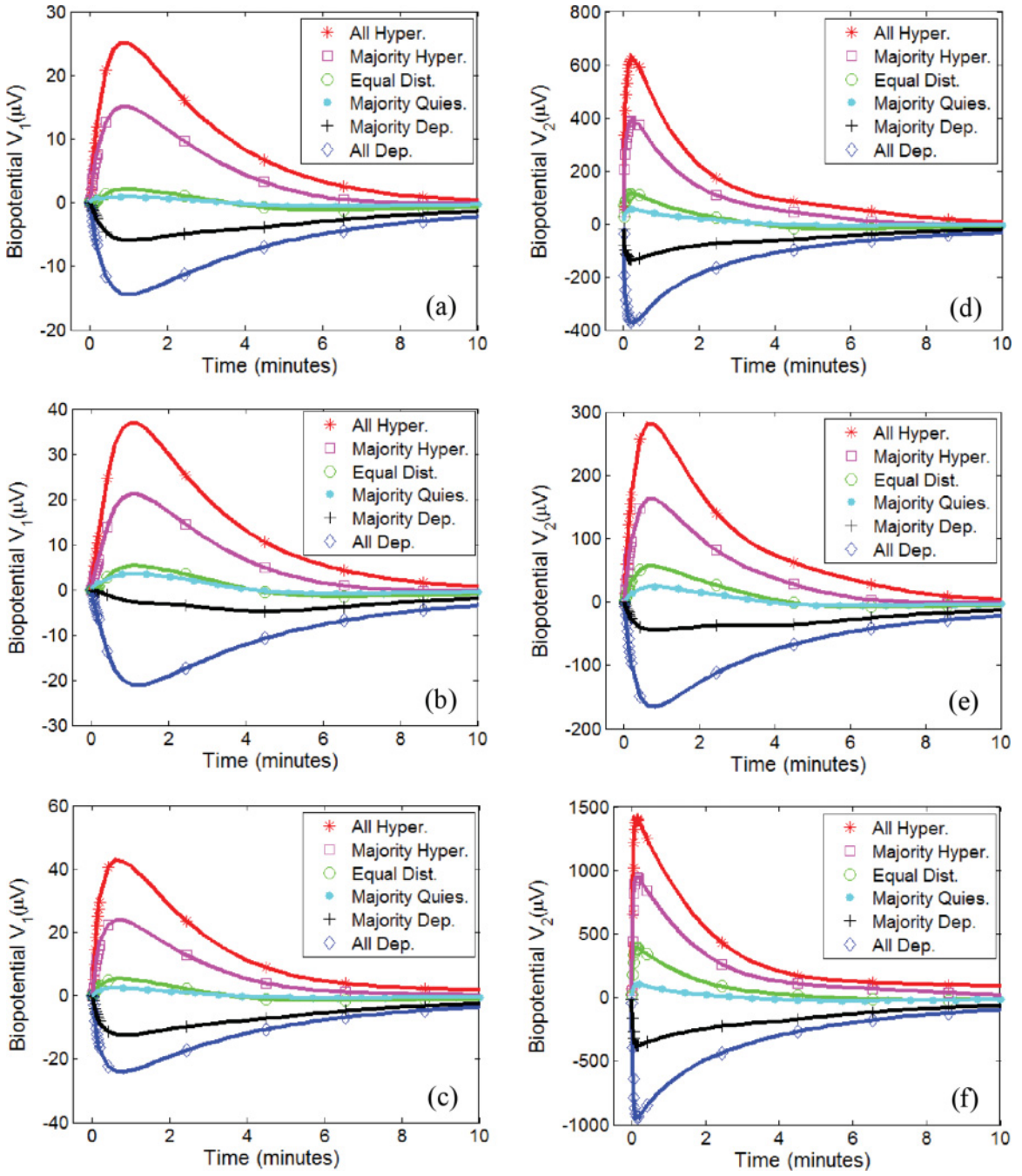

FIG. 8. (Color online) The biopotential differences V_1 generated by the (a) first papillary pattern, (b) first comedo pattern, and (c) first compact pattern and the biopotential differences V_2 generated by the (d) first papillary pattern, (e) first comedo pattern, and (f) first compact pattern. Total of 444 cells is used in each curve.

33%. Figure 6(e) shows Case 5, where the majority of cells are set to hyperpolarize by setting the probability of cells hyperpolarizing to 66.6%, the probability of cells depolarizing to 16.6%, and the probability of cells quiescent to 16.6%. Figure 6(f) shows Case 6, where all cells are hyperpolarizing. The different percentages of the cells in each transition were chosen empirically to study a variety of cases where the cells are equally distributed among the transitions, 33% of the cells in each transition, and the cases where the majority of the cells, 66%, are in a certain transition. In Figs. 6(b)–6(e), the black squares represent the quiescent cells, the dark gray squares represent the hyperpolarizing cells, and the white squares represent the depolarizing cells. Quiescent cells are neither depolarizing nor hyperpolarizing and, therefore, do not generate any extracellular biopotentials.

By comparing Fig. 6(a), all cells are depolarizing, with Fig. 6(f), all cells are hyperpolarizing, it can be seen that the hyperpolarization transition generates extracellular biopotentials larger in magnitude than the depolarization transition. In addition, in Fig. 6(d), the probability of a cell depolarizing is equal to the probability of a cell hyperpolarizing; however, the extracellular biopotentials are mostly

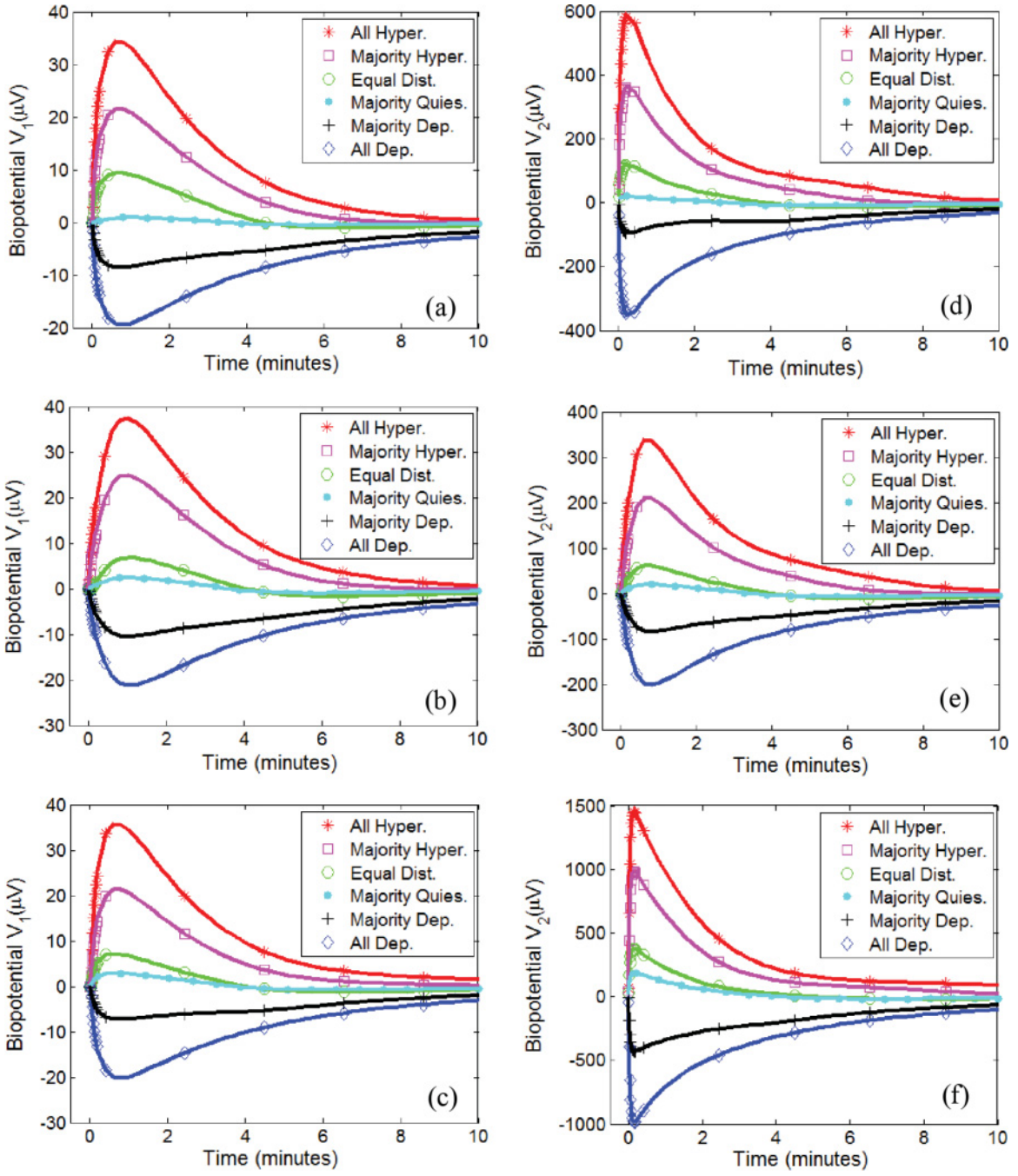

FIG. 9. (Color online) The biopotential differences V_1 generated by the (a) second papillary pattern, (b) second comedo pattern, and (c) second compact pattern the biopotential differences V_2 generated by the (d) second papillary pattern, (e) second comedo pattern, and (f) second compact pattern. A total of 444 cells is used in each curve.

positive, which indicates that the hyperpolarization dominates the depolarization transitions as discussed in our previous work [22–25].

In Fig. 6(b), where the majority of the cells are depolarizing, lower extracellular biopotentials are generated in comparison to the case where all the cells are depolarizing in Fig. 6(a). Also, in Fig. 6(e), where the majority of the cells are hyperpolarizing, lower extracellular biopotentials were generated than the case when all the cells are hyperpolarizing in Fig. 6(f). In Fig. 6(c), where the majority of the cells are quiescent, the extracellular biopotentials drop significantly compared to all the other cases, as anticipated.

More importantly, randomly distributing the cells at different cell division stages causes the spatial distribution of the extracellular biopotential to shift its peak, as shown in Fig. 6(c), where the biopotential distribution is shifted downward. This shift is further exemplified in Fig. 7 for the first comedo pattern which shows that the peak biopotential at the tissue boundary ($x = 0$) is different in the case when all the cells are depolarizing in comparison to the case when only the majority

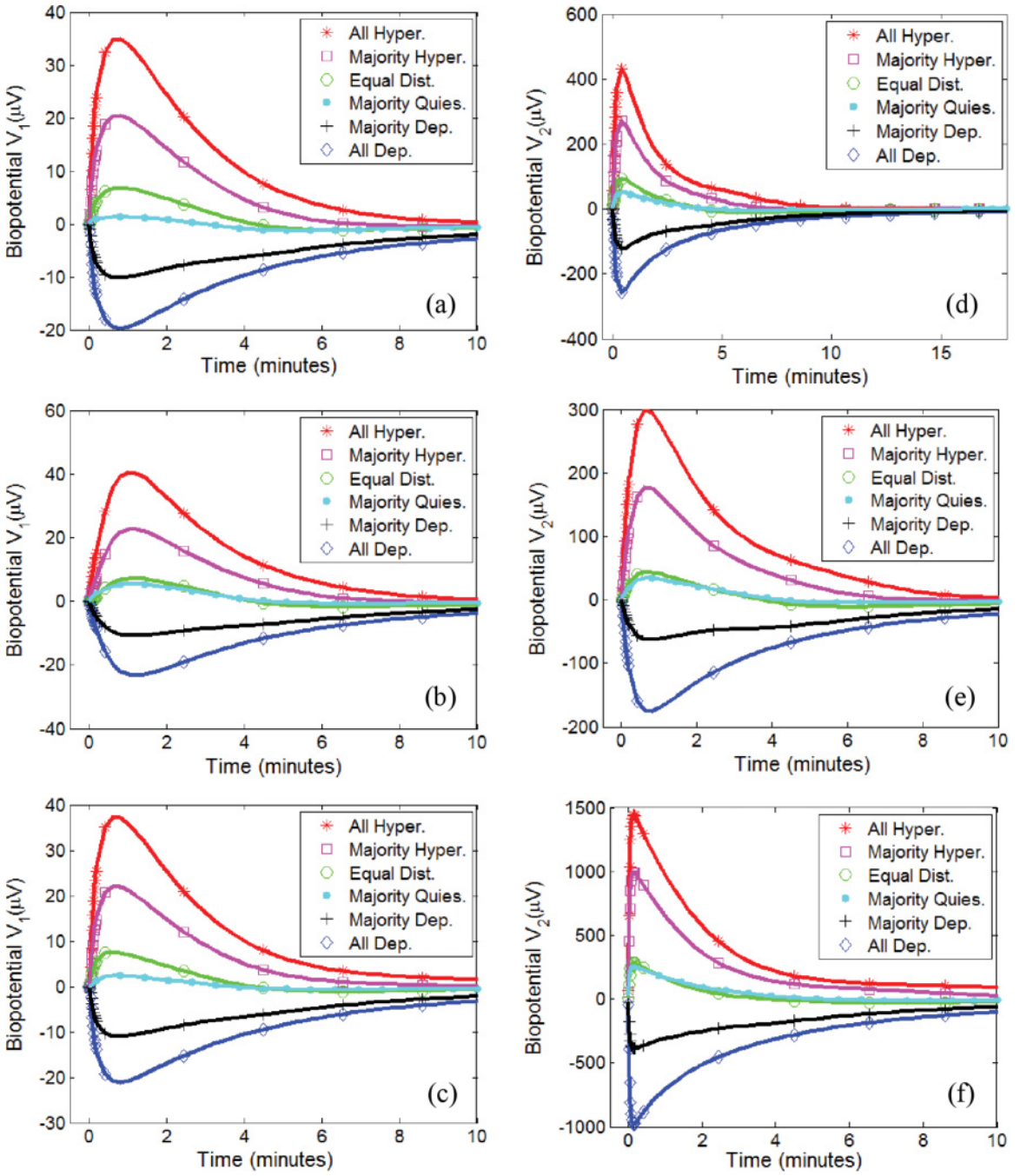

FIG. 10. (Color online) The biopotential differences V_1 generated by the (a) third papillary pattern, (b) third comedo pattern, and (c) third compact pattern and the biopotential differences V_2 generated by the (d) third papillary pattern, (e) third comedo pattern, and (f) third compact pattern. A total of 444 cells is used in each curve.

of the cells are depolarizing. This observation is important because in the reported biopotential detection clinical trials [11–20], a single sensor was placed on top of the center of the tumor and four other sensors were placed 2 cm to the left, right, top, and bottom of the center of the tumor [11–20]. Biopotential differences were then measured in these clinics and the presence of significant biopotential differences between the center electrode and the four other electrodes was used as an indicator to the presence of a tumor [11].

Most of the results in Figs. 6 and 7 indicate that the center sensor records the highest biopotential signal, which is in agreement with the clinical trials in Ref. [19]. However, few cases in Figs. 6 and 7, specifically Figs. 6(c) and 7(b), indicate that the point of maximum biopotential might be slightly shifted away from the center. Therefore, we propose to add more sensors in the array to capture possible higher peaks. More types of tumors; other than papillary, compact and comedo; and more cell division stage distributions need to

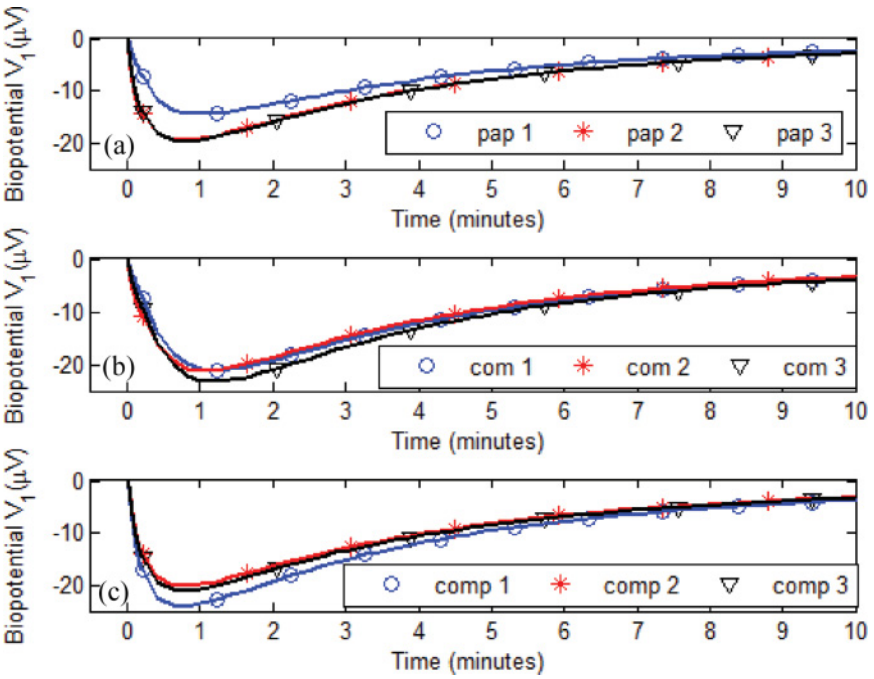

FIG. 11. (Color online) The biopotential V_1 generated by tumors in Case 1, all the cells depolarizing, for the (a) papillary pattern in Sets 1–3, (b) comedo pattern in Sets 1–3, and (c) compact pattern in Sets 1–3.

be investigated in the future to accurately determine the ideal sensor placement.

B. Temporal biopotential patterns

The results in the previous subsection show the spatial distribution of the biopotentials for different tumor patterns and at different cell division stages. This section is concerned with investigating the temporal patterns of the generated biopotentials. Two biopotential differences V_1 and V_2 are considered, as indicated in Fig. 2. The biopotential difference V_1 is calculated at the tissue boundary and it resembles the measurements performed on the surface of the breast in clinical trials [11–20]. The two points defining V_1 are positioned on the tissue boundary such that one point is placed approximately near the center of the tumor and the other point is placed away from the center of the tumors. The biopotential V_2 is defined such that one point is placed directly inside the center of the tumor and the other point is placed at the tissue boundary (see Fig. 2). Studying V_2 helps explain the motion of charges from the tumor vicinity to the tissue boundaries or the breast surface.

For Set 1 of tumor patterns shown in Figs. 1(a)–1(c), the biopotential differences V_1 and V_2 in all cases are plotted in Fig. 8. For Set 2 of tumor patterns shown in Figs. 1(d)–1(f), V_1 and V_2 are plotted in Fig. 9. For Set 3 of tumor patterns shown in Figs. 1(g)–1(i), V_1 and V_2 are plotted in Fig. 10. By considering the positive peaks of the papillary pattern in Fig. 8(a), it can be seen that the highest peak is achieved when all cells are hyperpolarizing (Case 6), followed by the case when the majority of the biopotentials are hyperpolarizing (Case 5), followed by the case when it is equally probable for the cells to be hyperpolarizing, depolarizing, or quiescent (Case 4), and then, finally, the case when the majority of the cells are quiescent (Case 3). As for the negative peaks of the papillary patterns, the case when all of the cells are depolarizing (Case 1) generated the largest magnitude followed by the case when the majority of the cells are depolarizing (Case 3). This trend is also observed in the comedo and compact patterns in Figs. 8(b) and 8(c). In most of the results of V_1, the trend was a rapid increase, either positive or negative, followed by a slow decay to zero. However, in some cases, such as in Case 2 of the first comedo pattern in Fig. 8(b) when the majority of the cells are depolarizing, the biopotential V_1 exhibits an unusual trend involving two maxima followed by a gradual decay to zero. These double maxima can be attributed to the heterogeneity in the division stages of the cancerous cells composing the tumor and to the distribution of the cancerous cells over a relatively large area. The biopotential contributions of cells at different locations will then arrive at different times at the points where V_1 is calculated causing the unusual trend shown in Fig. 8(b).

For V_2 in Figs. 8–10, it can be seen that V_2 is significantly larger, at least 10 times, than the biopotential V_1 since it is directly calculated at the center of the tumor. However, V_1 is calculated at the tissue boundary and the ion imbalance, caused by the ions discharged by the cancerous cells, dissipates significantly before the ions reach the boundary. Moreover, the peaks of V_2 occur at earlier times than the peaks of V_1 since the ions discharged by the cancerous cells require time to propagate to the tissue boundary ($x = 0$). Figures 8–10 show that the compact patterns generate the largest V_2 followed by the papillary patterns and then the comedo patterns. The reason behind this trend is that in defining V_2, the point inside the interior of the tumors is basically inside the necrotic core of the comedo pattern where the motion of the ions is least constricted.

To isolate the effect of the tumor shape from the effect of the different cell division stages, Fig. 11 shows V_1 for only the cases where all cells depolarizing. Figure 11(a) shows the biopotential V_1 for the three papillary patterns, Fig. 11(b) shows the biopotential V_1 for the three comedo patterns, and Fig. 11(c) shows the biopotential V_1 for the three compact patterns. By focusing on the peak of each curve in Fig. 11, it

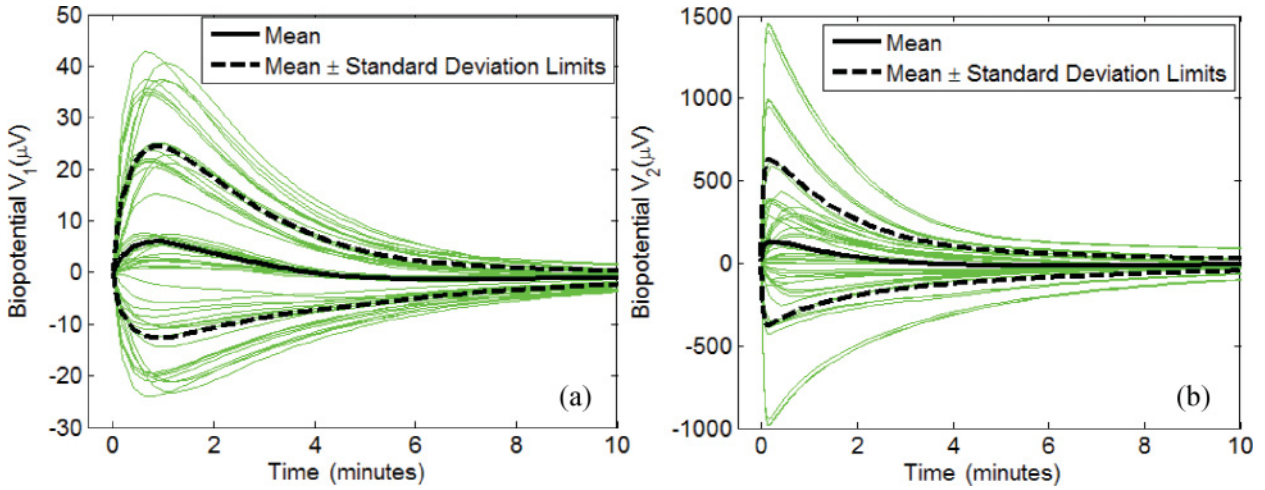

FIG. 12. (Color online) The biopotential differences (a) V_1 and (b) V_2 versus time for the 54 simulated cases from Sets 1–3 and Cases 1–6. The averages and the standard deviations are outlined in thick black lines.

can be seen that the minimum peak is generated by the papillary 1 pattern, at a value of -14.4 μV, and the maximum peak is generated by the compact 1 pattern, at a value of -24.1 μV. Overall, the tumors in the papillary category generated lower V_1 in comparison to the comedo and compact patterns which generated comparable values.

The biopotential differences V_1 and V_2 are plotted in Figs. 12(a) and 12(b), respectively, for all 54 considered cases simulated in this work. The average and the biopotentials at plus or minus one standard deviation are also plotted in Fig. 12. The results show that different tumor morphology and different cell division stages affect the biopotential signals at the tissue boundary represented by V_1 and the biopotential signals near the vicinity of the tumor represented by V_2. Therefore, tumor morphology and cell division stages can be one of the main factors contributing to the large variations observed in the recorded data from breast cancer patients [11].

Each of the curves (thin green lines) in Fig. 12(a) can also represent the recordings from a patient at different times. In Fig. 12(a), the curves with large positive amplitudes are generated at a time instant where the majority or all the cells are hyperpolarizing, the curves with large negative amplitude are generated at a time instant where the majority or all the cells are depolarizing, and the curves with the lowest amplitude, whether positive or negative, are generated at the time instant where a significant portion of the cancer cells are quiescent. If the biopotential recording is performed at the time instant when the majority of the cells are quiescent the malignant tumor might be missed since the signal will be too low. If the recording is repeated at a later time instant where the cancer cells have progressed to the stage where they are hyperpolarizing a much larger signal will be detected. Therefore, repeating the measurement or increasing the duration of the recording over time is anticipated to increase the accuracy of detection in future clinical trials.

C. Steady biopotential signals

In all previous examples, we assumed that all cancer cells start the depolarization or the hyperpolarization transitions at the same time; that is, all cells are synchronized. Realistically, cancer cells of a tumor do not divide synchronously [35]. In this section, the 444 cells of the first papillary pattern shown

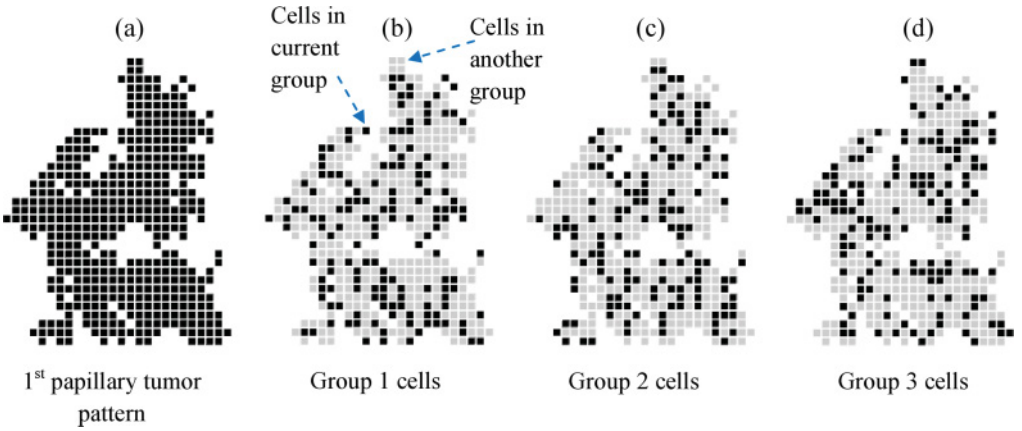

FIG. 13. (Color online) (a) The first papillary tumor pattern divided into (b) Group 1 (151 cells), (c) Group 2 (146 cells), and (d) Group 3 (147 cells). In (b)–(d) the cells composing each group are shown as black squares.

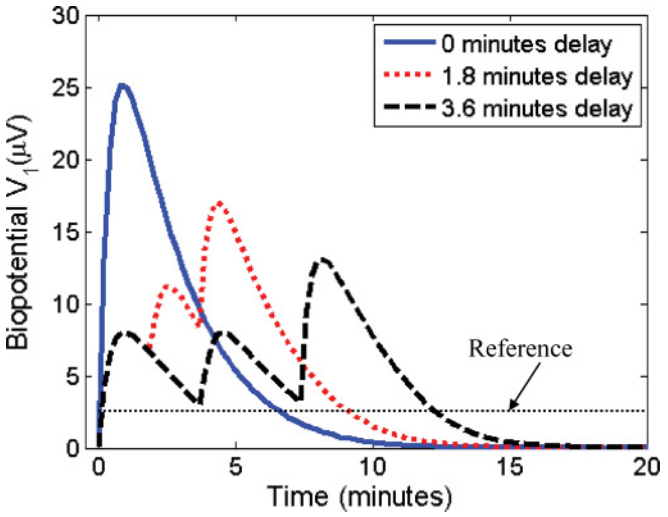

FIG. 14. (Color online) The biopotential V_1 generated by the first papillary tumor pattern where all cells are hyperpolarizing. Three cases are shown: (i) The case where all cells are hyperpolarizing simultaneously (solid blue curve). (b) The case where the cells are divided into three equal groups of cells (red dotted curve). The first group of cells starts the hyperpolarization transitions at 0 min followed by the second group, which starts the transition after 1.84 min, and, the third group starts the transition after 3.68 min. (c) The case where the cells are divided into three equal groups (black dashed) with a delay of 3.68 min versus 1.84 min in (b).

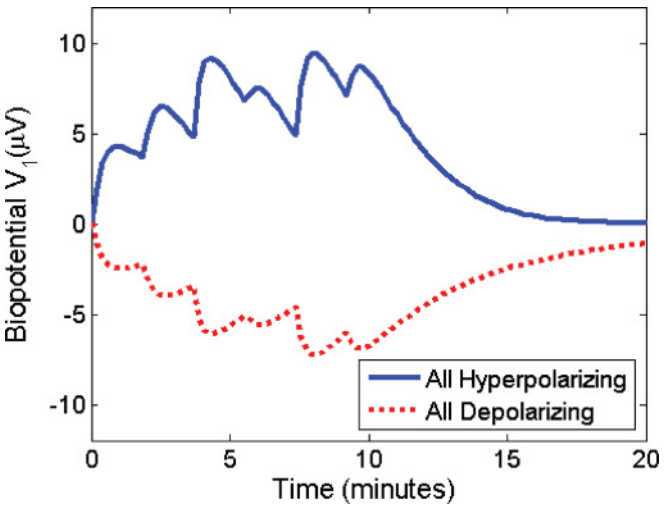

FIG. 15. (Color online) The biopotential V_1 generated by the first papillary tumor pattern when (a) all cells are hyperpolarizing (solid blue curve) (b) all cells are depolarizing (red dotted curve). For both cases, the cancer cells are divided into six randomly arranged groups with the first group starts the transition at 0 min, the second groups start after 1.84 min, the third group after 3.68 min, etc. Groups 1, 2, 3, 4, 5, and 6 consist of 69, 71, 82, 78, 74, and 70 cells, respectively.

in Fig. 1(a) [repeated in Fig. 13(a)] are divided into three randomly spatially arranged groups as shown in Figs. 13(b)–13(d). The idea is to investigate the effect of cells dividing at different time instants on the biopotential signals. For each cell, a random number, x, is generated between 0 and 1. If the random number is in the range between 0 and $1/3$, the cell is assigned to Group 1; between $1/3$ and $2/3$, the cell is assigned to Group 2; and between $2/3$ and 1, the cell is assigned to Group 3. The random generator was executed only once, leading to slightly different number of cells in each group.

Therefore, Group 1 in Fig. 13(b) includes 151 cells, Group 2 in Fig. 13(c) includes 146 cells, and Group 3 in Fig. 13(d) includes 147 cells. The cells in these three groups are incorporated in the diffusion-drift algorithm to compute the biopotential signals. The results of Fig. 14 are associated with the case where all cells are hyperpolarizing. The solid blue curve represents the case where all the 444 cells start hyperpolarizing at the same instant (i.e., synchronized). The dotted red curve and the dashed black curve represent the cases where the 444 cells are randomly spatially divided into the three groups shown in Fig. 13. The time delay between the three groups is 1.84 and 3.68 min for the dotted red and dashed black curves, respectively. As shown in Fig. 14, a reference threshold is selected to represent 10% of the maximum value of the solid blue curve.

The results demonstrate that the duration of the biopotential signal V_1 increases when cancer cells are nonsynchronized, as shown in Fig. 14. Specifically, the 1.84 min delay case (dotted red curve) and the 3.68 min delay case (dashed black curve) dropped below the reference value after 9.13 and 12.31 min, respectively, compared with the 6.19 min in the case where all the cells are synchronized (solid blue curve). When cancer cells are divided into more groups, the time duration of signal is expected to increase as shown in Fig. 15. In this case, cancer cells are divided into six randomly spatially arranged groups. These groups consist of 69, 71, 82, 78, 74, and 70 cancer cells, respectively. Assigning the cells to each group is conducted using the same mechanism of Fig. 13, where only three groups were used. In this case, the ranges of the random number in each of the six groups are 0 to $1/6$, $1/6$ to $2/6$, etc.

The solid blue curve in Fig. 15 represents the case where all cells are hyperpolarizing with a time delay between each group of 1.84 min. The dotted red curve represents the case where all cells are depolarizing with the same delay between the groups. As expected, the results of Fig. 15 show a longer duration in the biopotential signals V_1 for both transitions.

The results in this section demonstrate that steady or dc biopotential signals can be generated when cancer cells are dividing at different time instants. These results are in agreement with the recorded data from breast cancer patients [10–20]. Realistically, a cancer tumor can include a random mix of depolarizing and hyperpolarizing cells; therefore, it is anticipated that the amplitudes of the generated biopotential signals can have values between the two limits shown in Fig. 15.

IV. CONCLUSIONS

The diffusion-drift model was used to simulate the spatial and temporal evolution of biopotential signals generated by MCF-7 breast cancer cells. The algorithm was developed and parallelized in our previous work [21–24], where few numbers of cells were incorporated in the model. In this work, the cancer cells were spatially arranged to simulate well known breast cancer tumor patterns such as papillary, comedo, and compact tumors. The obtained results show that different tumor morphologies have significant impacts on

the spatiotemporal properties of the generated biopotentials. Specifically, the biopotentials signals exhibit elevated values in the regions where the motion of the ions is restricted, leading to increased accumulation of charges and, therefore, elevated biopotentials. This restriction of the motion of ions can explain the elevated biopotentials in the necrotic cores of the comedo patterns. In another example, because the compact pattern has the highest cell density, it generates the largest amplitudes of the biopotential signals. In addition, the biopotential amplitudes inside the tumor are observed to be at least one order of magnitude larger than those outside the tumor.

The algorithm is used to compute the biopotential signals from a mix of variety of cancer cell divisions. The total number of cells was randomly divided into several transition stages, that is, hyperpolarization, depolarization, and quiescent. In this work, six cases were simulated: all cells hyperpolarizing; all cells depolarizing; 66% of the cells hyperpolarizing, 16% depolarizing, and 16% quiescent; 66% of the cells depolarizing, 16% hyperpolarizing, and 16% quiescent; 66% of the cells quiescent, 16% depolarizing, and 16% hyperpolarizing; 33% of the cells hyperpolarizing, 33% depolarizing, and 33% are quiescent. The statistical average and standard deviation of the biopotential signal obtained using the results of all six cases for all nine tumor patterns is calculated. The obtained results show that, on average, a positive value of the biopotential signal is produced, which indicates that the hyperpolarization transition is dominating the mechanism. The computed standard deviation of the biopotential signal is observed to be large, which agrees with the reported values from clinical trials [11]. Finally, the results show large temporal variations in the biopotential signals, which suggest that increasing the duration of recording these signals may lead to an increase in the sensitivity of the detection technique.

The cancer cells are finally divided randomly (from the distribution point of view) into several groups. These groups exhibit time delays in the division transition of the included cancer cells. Almost steady biopotential signals (at least over a longer period of time) were observed. These results can justify the use of dc optimized electrodes for recording the signals in clinical trials [10–20].

In this work, nine tumor patterns were considered using the same number of cells. All tumors were located at the same position in the computational domain. Advanced parallelization techniques, such as the graphics processing units, will be explored in order to simulate larger tumor sizes, larger computational domains, and a variety of tumor depths. The signal to noise ratio will be investigated by corrupting the biopotential signals with random and additive noise, to mimic possible clutter from nearby organs. In addition, animal models implanted with MCF-7 cells will be used to validate the biopotential results obtained in this work.

ACKNOWLEDGMENTS

This work is funded in part by the Doctoral Academy Fellowship at the University of Arkansas and in part by NSF/EDA Award No. 0965571 (2010 Advances in Breast Cancer Research Workshop), Cyberinfrastructure Awards No. NSF/EPS 0918970 (CI TRAIN) and No. NSF/MRI #072265 (Star of Arkansas). The authors would also like to acknowledge Dr. David Zaharoff for his fruitful discussion.

APPENDIX A: MULTIPLE NUTRIENTS TUMOR GROWTH MODEL

The Ferreira *et al.* model includes two nutrients, one necessary for the metabolism of cancerous cells M and one necessary for cancerous cell division N. These nutrients are consumed by both cancerous and healthy cells at different rates. Specifically, healthy cells consume α normalized values per unit time from both nutrients N and M, whereas cancerous cells consume $\lambda_N\alpha$ and $\lambda_M\alpha$ normalized values per unit time from nutrients N and M, respectively.

At each time step, the values of the nutrients N and M are updated and two cell dynamics are implemented: (i) cell division and (ii) cell death. The probability of a cell dividing is expressed as a function of the nutrient N, whereas the probability of a cell dying is expressed as a function of the nutrient M as in Ref. [26].

Three tumor shape types were generated using the model of Ferreira *et al.* [26] as (i) *papillary*, (ii) *compact*, and (iii) *comedo*, which is a tumor with a central necrotic core. Mainly, three parameters control the shape of the generated tumor pattern as α, λ_{N}, and λ_{M}. Due to the increased computational demands to compute the biopotential signals from the generated tumor patterns, a square lattice size of 60×60 is used here, while in Ref. [26] the square lattice size was 501×501. The parameter α, defined as a function of the square lattice size, was varied from $1/500$ to $4/500$ in Ref. [26], while in this work, α was modified to range from $1/59$ to $4/59$ depending on the desired tumor pattern to be generated. As for λ_{N} and λ_{M}, they were varied from 25 to 200 and from 10 to 25, respectively, in Ref. [26], while they are varied from 200 to 250 and from 10 to 220, respectively, in this work. The elevated range for λ_{M}, up to 220, was only employed in the comedo tumor pattern as the smaller size of the square lattice used here necessitated the use of a higher value of λ_{M} in order to generate a necrotic core in the tumor pattern. It is important to emphasize that the work in Ref. [26] was to generate various tumor patterns while the work here is to solve the nonlinear equations of (1) to compute the biopotential signals and the electric current densities produced from the generated tumor patterns.

In this work, the parameters used to generate the papillary, comedo, and compact tumor patterns are ($\alpha = 0.05$, $\lambda_{\mathrm{N}} = 250$, $\lambda_{\mathrm{M}} = 20$), ($\alpha = 0.032$, $\lambda_{\mathrm{N}} = 220$, $\lambda_{\mathrm{M}} = 220$), and ($\alpha = 0.016$, $\lambda_{\mathrm{N}} = 200$, $\lambda_{\mathrm{M}} = 10$), respectively. A uniform intercellular spacing of $0.25\ \mu$m is inserted between the cells as estimated in Ref. [22]. Moreover, each pixel in the tumor pattern generated by the Ferreira *et al.* model could hold more than one cancerous cell. However, the 2D diffusion-drift model can only have a single cell at any position. Therefore, the pixels with more than one cancerous cell are identified and the number of cancerous cells at these pixels is modified to one. This will modify the number of cancerous cells generated by the Ferreira *et al.* but not the tumor morphology.

In order to have a fair comparison between the biopotential signals generated by the different tumor patterns, each pattern has to have the same number of cancerous cells and the same center position. Due to the randomness of the cellular activities incorporated in the Ferreira *et al.* tumor growth model, it is impossible to enforce the number of cells in each tumor pattern generated. However, the Ferreira *et al.* model parameters can be specified such that the papillary, compact, and comedo patterns have approximately the same number of cells. A certain number of cells, less than 5% of the total number of cells in any tumor pattern, is then added or removed to equalize the number of cells in all patterns. Finally, the positions of the cancerous cells are then shifted such that all the tumor patterns have the same center which is the center of the domain employed in the diffusion-drift model.

APPENDIX B: DIFFUSION-DRIFT MODEL SYSTEMS OF EQUATIONS

The matrix of the biopotential system of equations in Eq. (5a) is highly sparse, with the majority of rows containing only five nonzero entries as follows [22–24]:

$$A_\phi(k,(i-1)\times LL_x+j) = -\frac{2}{h_{i,j}h_{i,j+1}} - \frac{2}{g_{i,j}g_{i,j+1}} - \frac{F}{\varepsilon}\Delta t\sum_m\left[\frac{Z_m^2\mu_m(i,j+0.5)}{(h_{i,j}+h_{i,j+1})/2}\times\frac{C_m^t(i,j+0.5)}{h_{i,j+1}} + \frac{Z_m^2\mu_m(i,j-0.5)}{(h_{i,j}+h_{i,j+1})/2}\times\frac{C_m^t(i,j-0.5)}{h_{i,j}} + \frac{Z_m^2\mu_m(i+0.5,j)}{(g_{i,j}+g_{i+1,j})/2}\times\frac{C_m^t(i+0.5,j)}{g_{i+1,j}} + \frac{Z_m^2\mu_m(i-0.5,j)}{(g_{i,j}+g_{i+1,j})/2}\times\frac{C_m^t(i-0.5,j)}{g_{i,j}}\right], \tag{B1}$$

$$A_\phi(k,(i-1)\times LL_x+j+1) = \frac{2}{(h_{i,j}+h_{i,j+1})h_{i,j+1}} + \frac{F}{\varepsilon}\Delta t\sum_m\left[\frac{Z_m^2\mu_m(i,j+0.5)}{(h_{i,j}+h_{i,j+1})/2}\times\frac{C_m^t(i,j+0.5)}{h_{i,j+1}}\right], \tag{B2}$$

$$A_\phi(k,(i-1)\times LL_x+j-1) = \frac{2}{(h_{i,j}+h_{i,j+1})h_{i,j}} + \frac{F}{\varepsilon}\Delta t\sum_m\left[\frac{Z_m^2\mu_m(i,j-0.5)}{(h_{i,j}+h_{i,j+1})/2}\times\frac{C_m^t(i,j-0.5)}{h_{i,j}}\right], \tag{B3}$$

$$A_\phi(k,(i)\times LL_x+j) = \frac{2}{(g_{i,j}+g_{i+1,j})g_{i+1,j}} + \frac{F}{\varepsilon}\Delta t\sum_m\left[\frac{Z_m^2\mu_m(i+0.5,j)}{(g_{i,j}+g_{i+1,j})/2}\times\frac{C_m^t(i+0.5,j)}{g_{i+1,j}}\right], \tag{B4}$$

$$A_\phi(k,(i-2)\times LL_x+j) = \frac{2}{(g_{i,j}+g_{i+1,j})g_{i,j}} + \frac{F}{\varepsilon}\Delta t\sum_m\left[\frac{Z_m^2\mu_m(i-0.5,j)}{(g_{i,j}+g_{i+1,j})/2}\times\frac{C_m^t(i-0.5,j)}{g_{i,j}}\right]. \tag{B5}$$

where $k=(i-1)\times LLx+j$. The elements of the vector b_ϕ are given by

$$b_\phi(k) = -\frac{F}{\varepsilon}\left\{\sum_m[Z_mC_m^t(i,j)+\Delta t\left[\frac{-Z_mD_m(i,j+0.5)}{(h_{i,j}+h_{i,j+1})/2}\times\frac{[C_m^t(i,j+1)-C_m^t(i,j)]}{h_{i,j+1}} + \frac{Z_mD_m(i,j-0.5)}{(h_{i,j}+h_{i,j+1})/2}\times\frac{[C_m^t(i,j)-C_m^t(i,j-1)]}{h_{i,j}} - \frac{Z_mD_m(i+0.5,j)}{(g_{i,j}+g_{i+1,j})/2}\times\frac{[C_m^t(i+1,j)-C_m^t(i,j)]}{g_{i+1,j}} + \frac{Z_mD_m(i-0.5,j)}{(g_{i,j}+g_{i+1,j})/2}\times\frac{[C_m^t(i,j)-C_m^t(i-1,j)]}{g_{i,j}} + \frac{Z_m[J_{a_{xm}}(i,j+0.5)-J_{a_{xm}}(i,j-0.5)]}{(h_{i,j}+h_{i,j+1})/2} + \frac{Z_m[J_{a_{ym}}(i+0.5,j)-J_{a_{ym}}(i-0.5,j)]}{(g_{i,j}+g_{i+1,j})/2}\right]\right\}. \tag{B6}$$

The entries of the other three systems of equations in Eqs. (5b)–(5d) can be defined similar to Eqs. (B1)–(B6). The parallel solution of the previous equations is detailed in Ref. [23].

[1] R. Siegel, E. Ward, O. Brawley, and A. Jemal, Ca-Cancer J. Clin. **61**, 212 (2011).
[2] S. Glück and T. Mamounas, Oncology (Williston Park) **24**, 1 (1982).
[3] W. Berg, L. Gutierrez, M. NessAiver, W. Carter, M. Bhargavan, R. Lewis, and O. Ioffe, Radiology **233**, 830 (2004).
[4] D. Blackiston, K. McLaughlin, and M. Levin, Cell Cycle **8**, 3527 (2009).
[5] J. Strobl, W. Wonderlin, and D. Flynn, Gen. Pharmac. **26**, 1643 (1995).
[6] W. Wonderlin, K. Woodfork, and J. Strobl, J. Cell. Physiol. **165**, 185 (1995).
[7] H. Ouadid-Ahidouch, X. Le Bourhis, M. Roudbaraki, R. Toillon, P. Delcourt, and N. Prevarskaya, Recept. Channels **7**, 345 (2001).
[8] H. Ahidouch and A. Ahidouch, J. Membr. Biol. **221**, 1 (2008).
[9] E. Klimatcheva and W. Wonderlin, J. Membr. Biol. **171**, 35 (1999).
[10] B. Weiss, G. Ganepola, H. Freeman, Y. Hsu, and M. Faupel, Breast Dis. **7**, 91 (1994).
[11] A. Marino, D. Morris, M. Schwalke, I. Iliev, and S. Rogers, Tumor Biol. **15**, 147 (1994).
[12] M. Faupel, D. Vanel, V. Barth, R. Davies, I.S. Fentiman, R. Holland, J. L. Lamarque, V. Sacchini, and I. Schreer, Eur. J. Radiol. **24**, 33 (1997).
[13] M. Fukuda, K. Shimizu, N. Okamoto,T. Arimura, T. Ohta, S. Yamaguchi, and M. L. Faupel, Jpn. J. Cancer Res. **87**, 1092 (1996).
[14] J. Cuzick *et al*., The Lancet **352**, 359 (1998).
[15] E. Y. K. Ng, W. K. Ng, L. S. J. Sim, and U. Rajendra Acharya, Comput. Biol. Med. **37**, 1121 (2007).
[16] E. Y. K. Ng and W. K. Ng, Med. Biol. Eng. Comput. **44**, 131 (2006).
[17] E. Y. K. Ng, W. K. Ng, and R. U. Acharya, J. Med. Eng. Technol. **32**, 40 (2008).
[18] E. Y. K. Ng, S. Vinitha Sree, K. H. Ng, and G. Kaw, Technol. Cancer Res. Treat. **7**, 269 (2008).
[19] S. Vinitha Sree, E. Y. K. Ng, G. Kaw, R. Acharya, and B. K. Chong, J. Med. Syst. **35**, 79 (2010).
[20] V. Sree Subbhuraam, E. Y. K. Ng, G. Kaw, R. Acharya U, and B. K. Chong, J. Med. Syst., doi:10.1007/s10916-010-9441-z.
[21] A. M. Hassan and M. El-Shenawee, IEEE Trans. Biomed. Eng. **56**, 2370 (2009).
[22] A. M. Hassan and M. El-Shenawee, IEEE Trans. Biomed. Eng. **57**, 2099 (2010).
[23] A. M. Hassan and M. El-Shenawee, J. Parallel Distrib. Comput. **71**, 1011 (2011).
[24] A. Hassan, Ph.D. dissertation, University of Arkansas, 2010.
[25] A. M. Hassan and M. El-Shenawee, *Proceedings of the IEEE International Symposium on Antennas and Propagation and USNC/URSI National Radio Science Meeting, Spokane, WA, USA, July 3–8, 2011* (IEEE, Spokane, WA, 2011), pp. 726–729.
[26] S. C. Ferreira, M. L. Martins, and M. J. Vilela, Phys. Rev. E **65**, 021907 (2002).
[27] A. M. Hassan and M. El-Shenawee, *Proceedings of the Annual Review of Progress in Applied Computational Electromagnetics, Niagara Falls, Canada, March 30–April 4, 2008* (ACES, United States, 2008), pp. 86–91.
[28] B. Capogrosso Sansone, P. P. Delsanto, M. Magnano, and M. Scalerandi, Phys. Rev. E. **64**, 021903 (2001).
[29] S. D. Shumate and M. El-Shenawee, IEEE Trans. Biomed. Eng. **56**, 1341 (2009).
[30] I. Ramis-Conde, M. Chaplain, and A. Anderson, Math. Comput. Modell. **47**, 533 (2008).
[31] P. Macklin and J. Lowengrub, J. Theor. Biol. **245**, 677 (2007).
[32] H. Lodish, A. Berk, P. Matsudaira, C. Kaiser, M. Krieger, M. Scott, S. Zipursky, and J. Darnell, *Molecular Cell Biology*, 5th ed. (Freeman, San Francisco, 2003).
[33] C. Mummery, J. Boonstra, L. Tertoolen, P. Van Der Saag, and S. De Laat, J. Cell. Physiol. **107**, 1 (1981).
[34] J. Boonstra, C. Mummery, L. Tertoolen, P. Van Der Saag, and S. De Laat, J. Cell. Physiol. **107**, 75 (1981).
[35] R. Sutherland, R. Hall, and I. Taylor, Cancer Res. **43**, 3998 (1983).